Journal of Petroleum Science and Engineering 161 (2018) 611–624

Contents lists available at ScienceDirect

Journal of Petroleum Science and Engineering

journal homepage: www.elsevier.com/locate/petrol

# Numerical well test model for caved carbonate reservoirs and its application in Tarim Basin, China☆

Yi-Zhao Wan [a,*], Yue-Wu Liu [b], Fang-Fang Chen [c], Neng-You Wu [a], Gao-Wei Hu [a]

[a] Qingdao Institute of Marine Geology, Qingdao 266071, China
[b] Institute of Mechanics, Chinese Academy of Science, Beijing 100019, China
[c] Research Institute of Petroleum Exploration and Development, Tarim Oilfiled Company, PetroChina, Korla 841000, China

ARTICLE INFO

*Keywords:*
Caved carbonate reservoir
Type curves
Numerical well test
Finite element method

ABSTRACT

The caved carbonate reservoir is a special and complex reservoir with different size cavities, which implies a strong heterogeneity. It is a big challenge to characterize such reservoirs. The dual-porosity model and radial composite model are the two most commonly used models for the interpretation of well test in caved carbonate reservoirs. However, more studies are needed to determine whether these models can be applied to this special and complex type of reservoir. In this paper, first we classify the log-log plots of test pressure into four types and analyze the characteristics of each type. The results show that the cavity controls the pressure response and that the above-mentioned models are not appropriate for the well test interpretation of caved carbonate reservoirs. We also developed a numerical well test model for caved carbonate reservoirs. The model includes two cases: a well drilled outside a cavity and a well drilled inside a cavity. The model's equations were solved by the finite-element method. We analyzed the pressure response of the developed model and found that the log-log plots for the model of a well outside a cavity are similar to that of the dual-porosity model, but the physical mechanisms of these two models are different. The model of a well inside a cavity is similar to the radial composite model except for a deviation in the distance of the well from the center of the cavity. Sensitivity studies show the size of the cavity, its permeability, and the distance from the well to the cavity are the main factors influencing the pressure response behavior. Two field examples of build-up pressure tests are provided to show how the proposed model can be used to understand the properties of caved carbonate reservoirs and characterize them.

## 1. Introduction

Carbonate reservoirs are widely distributed around the world. Carbonates account for 20% of the world's total sedimentary rocks, and 52% of the world's total oil and gas reserves. The recoverable reserve of carbonate reservoirs is about 143.45 billion tons oil equivalent. In China, there is about a third of the total land area containing carbonate rocks distributed across Tarim, Sichuan, Ordos Basin, and the North China area. Geological and recoverable reserves of Chinese carbonates amount to 2.335 billion tons and 419 million tons, respectively (Jiang et al., 2008).

Compared to other kinds of reservoirs, the caved carbonate reservoirs in the Tarim Basin of China are unique. They are buried at a deep depth (>6 km), have multiscale fractures and caves, and are poorly connected (Ran et al., 2014; Zhu et al., 2015). The most significant characteristics of the reservoirs are the “bead-like structures” (Fig. 1) on the seismic reflection profiles (Xiao et al., 2010). Many authors believe that this seismic reflection represents large-scale caves (Zhao et al., 2014). Drilling into a reservoir with bead-like seismic reflections often leads to drilling breaks of long distances and large amounts of mud leakage (Li et al., 2016). An oil field in the Tarim Basin has recorded drilling breaks in 23% of its wells, the longest being 29 m, and 63.7% of wells leak mud into the formation, with one instance of leak being as high as 3483.55 cubic meters.

The pores of the caved reservoir can be divided into three types: matrix, fractures, and caves. The main storage space is provided by the matrix. Cores reveal that the average porosity and permeability of reservoirs is 1.22% and 0.77 md, respectively. It is should be noted that core samples cannot be obtained from caves because of the leakage of mud and drilling breaks, indicating that the porosity and permeability

☆ Project supported by the Natural Science Foundation of China (Grant No. 41474119).
* Corresponding author.
*E-mail address:* yizhao_wan@126.com (Y.-Z. Wan).

https://doi.org/10.1016/j.petrol.2017.12.013
Received 13 July 2017; Received in revised form 17 November 2017; Accepted 5 December 2017
Available online 8 December 2017
0920-4105/

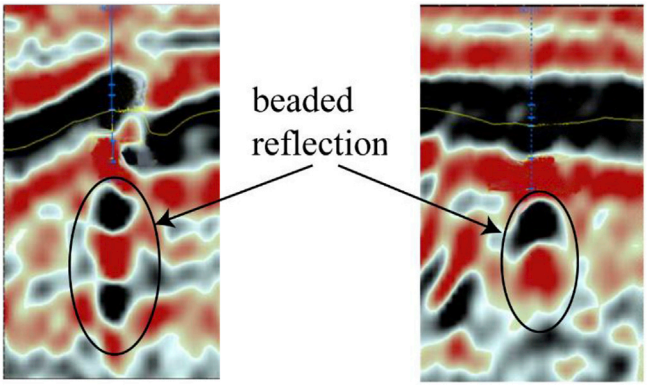


**Fig. 1.** Beaded reflection of caved reservoirs for a longitudinal seismic section.

from core data only represent the properties of the matrix. The concept of a "fracture-cave unit" (FCU) was first proposed by Jiao and Dou (2006a, 2006b), and is used to characterize fracture-cavity reservoirs and their internal fluid connectivity. An FCU refers to an assemblage of matrix, cavities, and fractures, and each unit is separated by continuous tight matrix zones. Also, an FCU refers to the body with uniform pressure and temperature, which can be viewed as "a reservoir" in a peculiar sense. FCU plays an important role in well spacing, calculation of geological reserves, evaluation of formation energy, and development scheme of fracture-cavity reservoirs (Ran et al., 2014). Fig. 2 shows a typical FCU, which consists of the cavities, fractures, and a matrix (Liu et al., 2011).

The description of the characteristics of reservoirs mainly relies on static data such as seismic inversion, core, logging, and other geological research data, but, these static methods are not accurate enough for production and dynamic forecasting. The boundaries of the cavity and the FCU in Fig. 2 can be determined by the amplitude and phase of seismic attributes, albeit with low precision (He et al., 2009). Well test analysis is a very important tool to dynamically evaluate parameters of a well and reservoir, which can then be combined with the static methods to verify geological models and improve the accuracy of reservoir description. Nevertheless, choosing the appropriate well test model is key to well test interpretation. Many examples in the literature and the well test report from Tarim Oil Field Company indicate that dual-porosity models and radial composite models are always the first choice for the interpretation of well tests in caved carbonate reservoirs (Wang et al., 2007; Nie et al., 2009; Djatmiko and Hansamuit, 2010; Gómez et al., 2014).

The dual-porosity model originates from the modeling of fractured reservoirs in the 1960s (Barenblatt et al., 1960; Warren and Root, 1963). The core concept of the dual-porosity model in fractured reservoirs is that

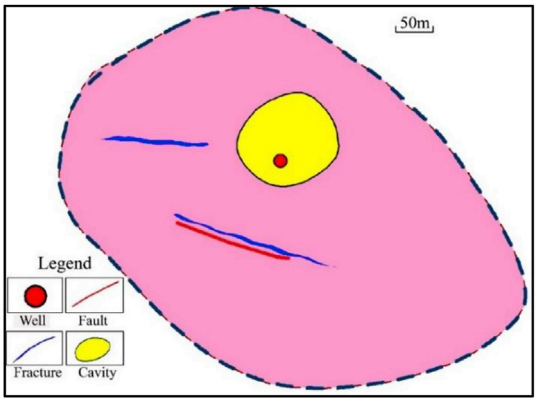


**Fig. 2.** Cross section of an FCU.

the permeability within fractures is significantly larger than that of the matrix, and thus, fractures represent the main paths for fluid transport. The matrix is the main storage space for fluid. Dual-porosity models use the geometrical perspective and assume that the reservoirs are divided into the auxiliary matrix and fractures. Two separate equations are proposed for the matrix and fracture subsystems. The two subsystems are connected by a matrix–fracture exchange term, which is the most important characteristic of a dual-porosity model. There are two types of exchange terms: steady state transfer functions (Barenblatt et al., 1960; Kazemi, 1969) and transient transfer functions determined by the transient flow equation within the matrix (de Swaan, 1976). Another important feature of the dual-porosity model is the shape of the matrix. The cubic block is the most commonly used matrix in the early stages. There are many other kinds of matrixes such as slabs, cylinders, and spheres. Different matrix shapes give rise to varied matrix–fracture exchange terms (Su et al., 2013). Many studies have also focused on inter-porosity flow (Najurieta, 1980; Civan and Rasmussen, 2001; Wan et al., 2016).

The radial composite model was first proposed for studying the pressure distribution in an infinite composite reservoir composed of two adjacent concentric regions of differing permeability (Loucks and Guerrero, 1961). It has been used to evaluate the efficiency of steam injection and in-situ combustion in a thermal oil recovery process (Satman et al., 1980a; 1980b). A steam zone with gradually increasing permeability is formed around the wellbore by steam injection or in-situ combustion. The zone outside the steam zone remains in the original state. Well test analysis of a radial composite model can be used to estimate the dynamic volume and permeability of the steam zone. Many radial composite models are proposed for well test analysis in different situations, such as fractured wells, water or air injection wells, and unconventional multi-fracture reservoirs (Chu and Shank, 1993; Stalgorova and Mattar, 2013; Gao et al., 2016; Yao et al., 2016).

When the dual-porosity model is applied to a caved carbonate reservoir by a well testing engineer, the cavities are considered to be the storage space of the fluid and the fractures are the paths of fluid transport. The matrix is assumed to be impervious because of the low permeability (Liu et al., 2011). Engineers prefer the dual-porosity model to analyze well test data from caved reservoirs for two reasons. First, caved reservoirs are characterized by multiple porosities, similar to the assumption of the dual-porosity model. The second, and more important reason, is that the log-log plots of the test pressure in some wells show characteristics consistent with the dual-porosity model (see the second row of Table 1). However, the large cavities dominate fluid flow and these cavities are too large to satisfy the assumptions of the dual-porosity model. When the radial composite model is applied in caved reservoirs, the inner zone represents the large cavities. The log-log plots of test pressure show the typical characteristics of the radial composite model, as well as the large mobility ratio of the inner zone to the outer zone (see the third row of Table 1). However, it is obvious that the radial composite model is only suitable when the well is located inside the cavity. Based on the above analysis, the dual-porosity model and radial composite model are not appropriate for the interpretation of well test data in caved carbonate reservoirs.

A notable fact is that there are two kinds of cavities in the reservoirs, filled and unfilled cavities. Most of the cavities are filled with argillaceous rocks and breccia. The theory of flow in porous media can be used to describe the fluid flow, but some cavities are vacant, and the Navier–Stokes equation controls fluid flow. In this paper, we only discuss the situation of cavities filled up with porous material and non-Darcy effect is not considered. Therefore, the flow in the filled cavities is consistent with Darcy's law. The case of filled cavities with non-Darcy effects and vacant cavities in which the fluid flow subject to the Navier–Stokes equation will be discussed in separate studies.

Many authors have noticed that large-scale cavities have a noticeable effect on the transient pressure response, especially when a well is drilled into them. Liu and Wang (2012) and Yang et al. (2011)

developed a simplified composite well testing model based on the assumption that the cavity is an equipotential body and the outer region is modelled by a dual-porosity model. Another model developed by Cheng et al. (2009) describes a cavity with a drilled well that acts as an expanded wellbore. Zhang et al. (2009) developed a well test model wherein a drilled cavity was treated as a Darcy flow region with a higher permeability. Gao et al. (2016) proposed a well test model including a filled cavity in which the well was drilled and the outer region were modelled using a dual-porosity model. They also considered the non-Darcy effect of the cavity, which can be described by the Barree–Conway model. These studies made a considerable contribution to the understanding of the pressure transient behavior of a well drilled into a cavity. Nevertheless, there is a lack of research focusing on wells drilled outside cavities.

In this paper, we classify the log-log plots of test pressure in the Tarim Basin into four types, based on the geological features and characteristics of pressure/pressure derivative curves. Then, using the classification of the log-log plots, we show that the most commonly used models (dual-porosity and radial composite) are not appropriate for the interpretation of well test data in caved carbonate reservoirs. A new model including a well inside a cavity and a well outside a cavity is proposed, and we use the finite element method to solve the governing equations of the model. We analyze the influence of the cavities' size, mobility, and distance between the well and the cavities on the behavior of the log-log type curve of bottom hole pressure. A comparison between the model proposed in this paper and the dual-porosity model shows how important it is to choose the correct model for the interpretation of test pressure data. Then, two field examples of build-up pressure tests interpreted by the model are presented.

**Table 1**
The classification of log-log plots of well tested pressure.

| Type | Log-log plots | FCU | *C/S* | *K* | Drilling event | Number of wells/ Percentage |
|---|---|---|---|---|---|---|
| I | 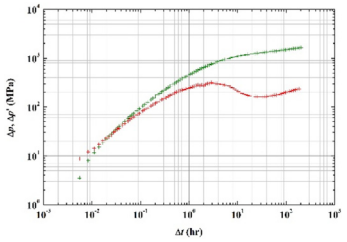 | 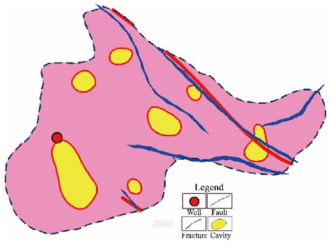 | $C<0.1$ $S>0$ | $K \propto 10$ mD | No drilling break, a small amount of mud leakage in some wells | 24/32.8% |
| II* | 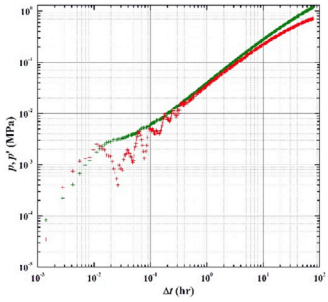 | 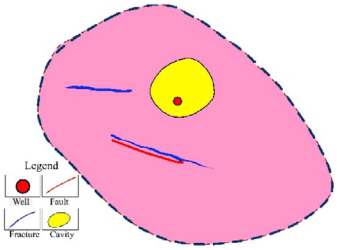 | $C > 10$ $S<0$ | $K_1$ [a] $> 1\,000$ mD $K_2$ [b] $< 0.1$ mD | Drilling break and leakage of mud occurred | 41/56.2% |
| III | 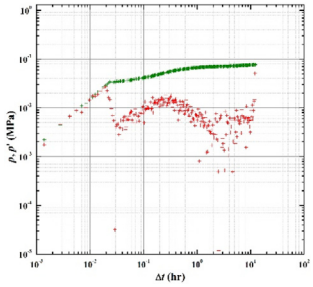 | 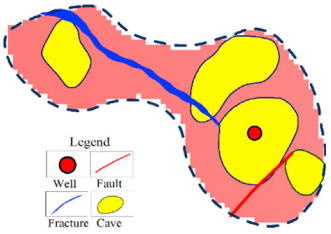 | $C > 10$ $S<0$ | $K > 1\,000$ mD | Drilling break and leakage of mud occurred | 4/5.5% |
| IV | 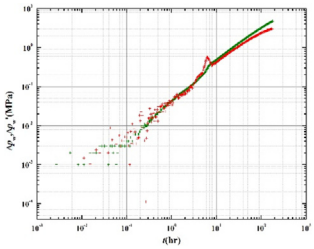 | 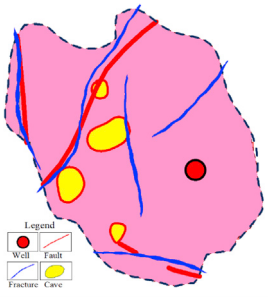 | $C > 50$ | $K < 0.1$ mD | No drilling break and mud leakage | 4/5.5% |

*Note: The parameters of the wellbore and reservoir have been calculated using the radial composite model.
[a] $K_1$ represents inner zone's permeability.
[b] $K_2$ is the outer zone's permeability.

## 2. Classification of log-log plots of the well test pressure

### 2.1. Criteria of the classification

As mentioned above, well test analysis is an effective tool to understand well and reservoir performance; however, it takes on the form of an inverse problem, to which there are multiple possible solutions. Therefore, it is important to combine other methods or data with well test analysis to reduce ambiguity. We classified the log-log plots of 73 wells in the Tarim Basin area. The classification had two purposes. The first was to recognize the pattern of test pressure and reduce ambiguity. The other was to establish the corresponding relationship between the geological features and log-log plots of test pressure, which can help engineers understand the reservoir geology.

We identified four factors of the classification criteria:

1 Geological features: Geological information is the static basis of classification. It mainly refers to the FCU (Fig. 2), which roughly shows the size and location of the cavities.
2 Events during the drilling process: As mentioned above, drilling break and leakage of drilling mud often occur during the drilling process. These are direct evidence of cavity existence and indicate whether the well has hit the cavity.
3 The morphological characteristics of the log-log plots: The type (valley, straight line, distance of pressure, and pressure derivative curve, etc.) of the log-log plots of test pressure reflect geological information. It is the most important basis for the classification.
4 Parameters of the wellbore and reservoir implied from the log-log plots: These parameters are derived from the results of the well test interpretation using the analytical models depending on the morphological characteristics. There parameters mainly refer to wellbore storage, skin, and permeability.

### 2.2. Description of the classification

On the basis of the above criteria, we classify the log-log plots of test pressure into four types, which are shown in Table 1. The characteristics of each type are as follows:

1 Type-I: Log-log plots of test pressure have a valley on the pressure derivative curve, which is similar to the response of the dual-porosity model. The wellbore storage coefficients are in the normal range, from 0.01 $m^3$/MPa to 1 $m^3$/MPa. The skin factor is positive. The FCU indicates that there are cavities within the unit but that the well is located outside the cavities. This type accounts for 32.8% of all the 73 wells.
2 Type-II: The log-log plots of test pressure show radial-flow with a short duration after the wellbore storage, with an increasing pressure curve and derivative curve toward the end of the test. The features of this log-log plot are consistent with the radial composite model with a large mobility ratio of the inner zone to the outer zone. Drilling breaks and mud leakage often occur in the drilling process of these type of wells. The wellbore storage coefficients are all larger than 10 $m^3$/MPa which is too large for a normal oil well. The skin factor is negative. The results interpreted by a radial composite model show the permeabilities of the inner zone are all larger than 1 000 md, correspondingly, the permeabilities of the outer zone are all smaller than 0.1 md or lower. From the FCU, we can see the well is located within the cavity. This type of plot accounts for 56.2% of all the 73 wells in the Tarim Basin Area.
3 Type-III: Log-log plots of test pressure have multiple peaks and valleys. The characteristics of wellbore storage and skin factor are similar to type-II, and also include drill breaks and mud leakage. The FCU indicates the presence of several large cavities, and the wellbore is located within one of them.
4 Type-IV: The pressure curve and derivative curve overlie each other. In this case, the wellbore storage is very large (more than 50 $m^3$/MPa).

### 2.3. Analysis of the classification

The analysis of the classification of log-log plots of test pressure leads us to conclude that cavities control the fluid flow. The main difference in the geological features between type I and type II is hinged on whether the well is located within a cavity, which causes the difference in the log-log plot of test pressure. Therefore, we believe that the valley on the derivative curve for type I is dominated by cavities with high permeability near the well. The type-II log-log plots are consistent with the radial composite model because the well is located within the cavity, which can be verified by the drilling break and leakage of mud. The cavity is located in the inner zone of the radial composite model, making the permeability of the inner zone very large; however, the permeability of the outer zone is very small because the zone lies outside is the matrix and has low permeability. Moreover, the cavity in which the well is located increases the effective radius of the wellbore. This is why wellbore storage is large and the skin factor is negative.

With regard to type III, the first valley on the derivative curve is caused by the cavity where the well is located, and the second valley is the response of the other cavity adjacent to the first. It is a combination of type I and type II. The production rate of this type can be as large as 150 t/d. More research is needed with regard to type III plots. Compared with the first three types, there are no large-scale cavities in the FCU of type IV. The log-log plots of tested pressure are still in the period of wellbore storage stage during the whole test because of the extremely low permeability of the matrix. We also noticed that type-I wells were almost always drilled at the early stages of oilfield development and type-II wells were drilled thereafter. This is because the wells of caved carbonate reservoirs are designed to penetrate cavities, but in the early stage, the coordinates of seismic data are inaccurate because of the lack of calibration, and thus, the well does not hit the cavity. The increase in the number of wells makes it easier to locate cavities and penetrate them.

On the basis of the above analysis, we can get an inference that the characteristics of the log-log plots in type I are not the response of the dual-porosity model. They are the response of the cavity. Let us refresh our memories regarding the dual-porosity model. The dual-porosity model assumes that each subsystem is distributed continuously and uniformly in the entire formation. From the perspective of continuum mechanics, any spatial point contains each subsystem at the same time. If we choose a representative elemental volume (REV) $\Delta V$ of the dual-porosity model (Fig. 3), the fracture and matrix will fill up with the REV. For heterogeneous media, there is a maximum REV ($\Delta V_{max}$). If the REV is too large, the physical parameters will change in response to changes in $\Delta V$. In other words, the scale of the cavities in the dual porosity model should be less than $\Delta V_{max}$. However, in caved carbonate reservoirs, the size of cavities is much larger than $\Delta V_{max}$. This is the theoretical explanation for the inapplicability of the dual-porosity models in caved carbonate reservoirs.

## 3. Mathematical models and numerical method

### 3.1. Description of the physical model

The analysis of the classification of the log-log plots indicates that cavities appear to be the principal factors that control the fluid flow and determine the characteristics of pressure response. Note also that the dual-porosity model is not appropriate for well test interpretation in caved carbonate reservoirs. Therefore, we develop a new model, mainly considering the influence of cavities. Depending on the location between the well and the cavity, two different cases arise: the well is located inside the cavity (WIC) and the well is located outside the cavity (WOC). Fig. 4 shows this geological model.

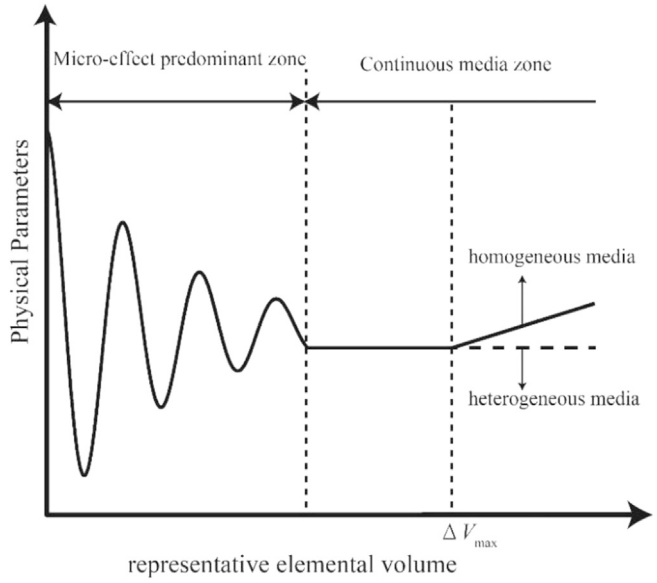


**Fig. 3.** The relationship between the physical parameters and the representative elemental volume (REV).

For the sake of simplicity, the cavity is represented by a circle. The zero-point is located in the wellbore. The radius of the cavity is $r_v$ and the distance from the cavity to the wellbore is $d$. We can find that if $d$ is larger than $r_v$, the model to be applied is that of the WOC; otherwise, we apply the WIC model.

A few assumptions are made to develop the mathematical models:

1 The formation is horizontal and has a uniform thickness. The top and bottom boundaries of the formation are impermeable.
2 Fractures are not explicitly considered. We assumed that the fractures are uniformly distributed in the reservoirs and they appear as part of the matrix (Teimoori, 2005). Also, we assume that the matrix is homogeneous based on two reasons. First, from the classification of Table 1, we believe that the valley on the derivative curve of Type-I is caused by the cavities not the dual-porosity effect. Second, there isn't any feature of dual-porosity model on the filed data of Type-II in Table 1 and the dual-porosity effect occurs very lately on the derivative and may not be recognized by the short time test. From the practical aspect, there is no need to consider the effects that are not recognized by the field test data.
3 The pore space of the formation is full of oil, which is assumed to be weakly compressible. The production rate of the well is constant.
4 The cavity is full of porous media. The flow in the cavity and other regions follows Darcy's law. (The case of a vacant cavity will be discussed in a future study).
5 The wellbore storage and skin are considered, but gravity, capillary pressure, and other physical and chemical effects are ignored.

### 3.2. Mathematical models

Based on the assumptions of the physical model, the governing equations of fluid flow through the reservoir regions described in Fig. 4 can be derived from mass conservation and Darcy's law.

The mass conservation for fluid in the matrix region is:

$$\frac{\partial(\phi_m \rho)}{\partial t} + \nabla\cdot(\rho\cdot \boldsymbol{V}_m) = 0 \tag{1}$$

where $\phi_m$ is the porosity of the matrix, $\rho$is the density of oil, $\boldsymbol{V}_m$is the seepage velocity in the matrix, and$t$is time.

The Darcy's law is:

$$\boldsymbol{V}_m = \frac{K_m}{\mu}\nabla p_m \tag{2}$$

where $p_m$ is the pressure in the matrix, $\mu$ is the viscosity of fluid, $K_m$ is the permeability of the matrix.

The state equations are:

$$\phi_m = \phi_{m0}\left[1 + c_\phi(p_m - p_{m0})\right] \tag{3}$$

$$\rho = \rho_0\left[1 + c_f(p_m - p_{m0})\right] \tag{4}$$

where $\phi_{m0}$ is the porosity of the matrix at the reference pressure $p_{m0}$, $\rho_0$is the density of fluid at the pressure$p_{m0}$, $c_\phi$is the compressibility coefficient of porosity, $c_f$is the compressibility coefficient of fluid.

Substituting equations (2)–(4) into equation (1), we get the diffusion equation of matrix pressure:

$$\frac{\partial^2 p_m}{\partial x^2} + \frac{\partial^2 p_m}{\partial y^2} = \frac{\phi_m \mu c_t}{K_m}\frac{\partial p_m}{\partial t} \tag{5}$$

where $c_t = c_f + c_\phi$, and we assume the matrix is isotropous.

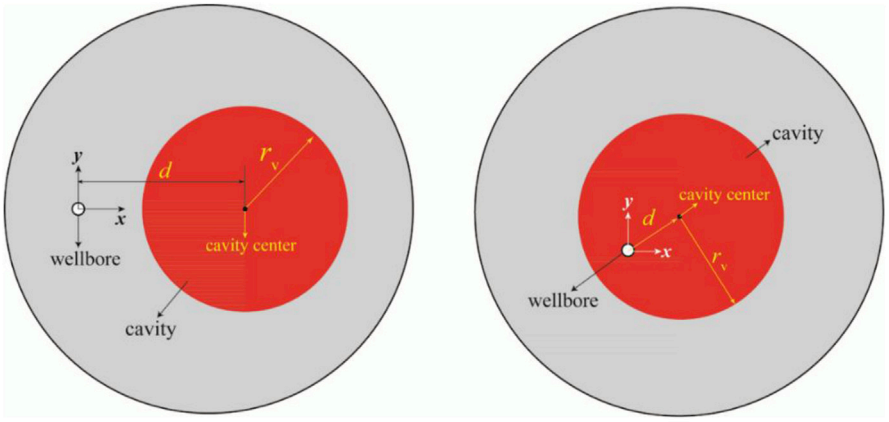


(a) well outside of a cavity(WOC) (b) well inside of a cavity(WIC)

**Fig. 4.** Planar view of the geological model with a cavity. The zero-point is located in the well. The radius of the cavity is $r_v$ and the distance from the center of the cavity to the wellbore is $d$. If $d > r_v$, the well will be located outside of the cavity (left); else, it will be located inside of the cavity (right).

In the same way, the diffusion equation of cavity pressure is:

$$\frac{\partial^2 p_c}{\partial x^2}+\frac{\partial^2 p_c}{\partial y^2}=\frac{\phi_c \mu c_t}{K_c}\frac{\partial p_c}{\partial t} \tag{6}$$

where $p_c$ is the pressure in the cavity, $\phi_c$ is the porosity of the cavity, and $K_c$ is the permeability of the cavity.

The initial conditions are that the pressure in the matrix and the cavity maintain the initial pressure$p_i$, that is:

$$p_c(t=0)=p_i, p_m(t=0)=p_i \tag{7}$$

The inner boundary condition considering wellbore storage effect can be given by the mass conservation in the wellbore boundary:

$$2\pi r_w h\frac{K_w}{\mu}\left(\frac{\partial p}{\partial n}\right)\Big|_{\Gamma_w}=Bq+C\frac{dp_w}{dt} \tag{8}$$

where $r_w$ is the wellbore's radius, $h$ is the formation's thickness, $K_w$ is the permeability on the boundary of wellbore which is represented by $\Gamma_w$ and it is $K_c$ when the well is inside of the cavity, or $K_m$ when the well is outside of the cavity, $(\partial p/\partial n)_{\Gamma_w}$ is the pressure gradient on the boundary $\Gamma_w$. $B$ is the volume factor of oil, $q$ is the production rate of the well, $C$ is the wellbore storage coefficient, and $p_w$ is the pressure on the boundary $\Gamma_w$

There are two types of reservoir boundary condition:

No fluid flow:

$$\left(\frac{\partial p_m}{\partial n}\right)_{\Gamma_r}=0 \tag{9}$$

or Constant pressure:

$$p_m|_{\Gamma_r}=p_i \tag{10}$$

where $\Gamma_r$ represents the boundary of the reservoir.

There are two conditions on the interface between the matrix and the cavity, which are the continuity of pressure and continuity of flow rate:

$$p_m|_{\Gamma_c}=p_c|_{\Gamma_c} \tag{11}$$

$$\frac{K_m}{\mu}\left(\frac{\partial p_m}{\partial n}\right)\Big|_{\Gamma_c}=\frac{K_c}{\mu}\left(\frac{\partial p_c}{\partial n}\right)\Big|_{\Gamma_c} \tag{12}$$

$\Gamma_c$ is the boundary of the cavity.

Equations (5)–(9) and (11) and (12) are the mathematical models. Then, we rewrite them in the dimensionless form considering skin effect. Variables in equations (1)–(12) are in SI units. When define the dimensionless form of the variables, we use the SPE preferred units referring to the section of nomenclature (The SI Metric System of Units And SPE METRIC STANDARD). Here are the dimensionless form of the variables:

$$p_{1D}=\frac{K_m h(p_i-p_m)}{1.842q\mu B},\ p_{2D}=\frac{K_m h(p_i-p_c)}{1.842q\mu B},\ x_D=\frac{x}{r_w e^{-s}},\ y_D=\frac{y}{r_w e^{-s}},\ t_D=\frac{3.6\times 10^{-3}K_m t}{\phi_m \mu c_t r_w^2},\ C_D=\frac{0.1592C}{\phi_m h c_t r_w^2},\ T_D=\frac{t_D}{C_D},\ d_D=\frac{d}{r_w e^{-S}},\ r_{vD}=\frac{r_v}{r_w e^{-S}}$$

where $p_{1D}$ is the dimensionless pressure of the matrix, $p_{2D}$ is the dimensionless pressure of the cavity, $S$ is the skin factor, $t_D$ is the dimensionless time, $C_D$is dimensionless wellbore storage coefficient, $d_D$ is dimensionless distance between the wellbore and the center of the cavity, $r_{vD}$ is the dimensionless radius of the cavity.

The dimensionless form the governing equations can be given by:

Matrix zone:

$$\frac{\partial^2 p_{1D}}{\partial x_D^2}+\frac{\partial^2 p_{1D}}{\partial y_D^2}=\frac{1}{C_D e^{2S}}\frac{\partial p_{1D}}{\partial T_D} \tag{13}$$

The governing equation for cavity zone is:

$$\frac{\partial^2 p_{2D}}{\partial x_D^2}+\frac{\partial^2 p_{2D}}{\partial y_D^2}=\frac{1}{DC_D e^{2S}}\frac{\partial p_{2D}}{\partial T_D} \tag{14}$$

where $D$ is the diffusivity ratio and the definition is:

$$D=\frac{(K/\mu\phi c_t)_c}{(K/\mu\phi c_t)_m} \tag{15}$$

Initial conditions:

$$p_{1D}(T_D=0)=0, p_{2D}(T_D=0)=0 \tag{16}$$

Wellbore boundary condition:

$$\frac{\partial p_D}{\partial n}\Big|_{\Gamma_w}=\left(-1+\frac{dp_{wD}}{dT_D}\right) \tag{17}$$

$p_D$ is $p_{1D}$ in the case of WOC and $p_{2D}$ in the case of WIC

Reservoir boundary conditions:

No fluid flow:

$$\frac{\partial p_{1D}}{\partial n}\Big|_{\Gamma_r}=0 \tag{18}$$

Constant pressure:

$$p_{1D}|_{\Gamma_r}=0 \tag{19}$$

The surface conditions between the matrix and the cavity are:

$$p_{1D}|_{\Gamma_c}=p_{2D}|_{\Gamma_c} \tag{20}$$

$$\frac{\partial p_{1D}}{\partial n}\Big|_{\Gamma_c}=M\frac{\partial p_{2D}}{\partial n}\Big|_{\Gamma_c} \tag{21}$$

where $M$ is the mobility ratio and the definition is

$$M=\frac{(K/\mu)_c}{(K/\mu)_m} \tag{22}$$

### 3.3. Numerical solutions

The geometric model is discretized into triangular elements which are presented in Fig. 5 by using the Open Source toolkit Netgen (Schöberl, 1997). We refine the mesh around the wellbore and in the cavity.

We use the Galerkin weighted residual method to discretize equations (13) and (14). The variational forms of these two equations are:

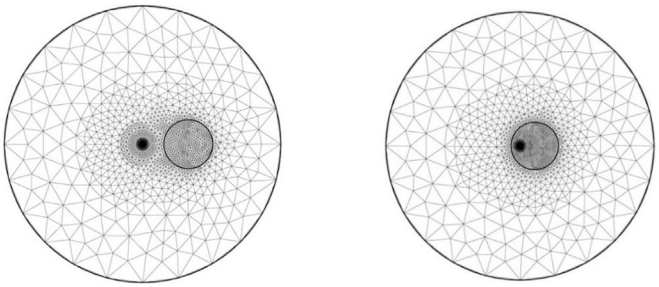

(a) mesh of WOC (b) mesh of WIC

**Fig. 5.** The mesh of the geometric model for numerical method. Meshes around the wellbore and the cavity are refined.

$$\iint_A \left( \frac{\partial^2 p_{1D}}{\partial x_D^2} + \frac{\partial^2 p_{1D}}{\partial y_D^2} - \frac{1}{C_D e^{2S}} \frac{\partial p_{1D}}{\partial T_D} \right) \delta p_{1D} dA = 0 \tag{23}$$

and

$$\iint_A \left( \frac{\partial^2 p_{2D}}{\partial x_D^2} + \frac{\partial^2 p_{2D}}{\partial y_D^2} - \frac{1}{DC_D e^{2S}} \frac{\partial p_{2D}}{\partial T_D} \right) \delta p_{2D} dA = 0 \tag{24}$$

where $\delta p_{1D}$ and $\delta p_{2D}$ are the variations of $p_{1D}$ and $p_{2D}$, respectively. $A$ is the area of one triangular.

equation (23) can be rewritten as:

$$\iint_A \left( \frac{\partial}{\partial x_D} \left( \frac{\partial p_{1D}}{\partial x_D} \right) \delta p_{1D} + \frac{\partial}{\partial y_D} \left( \frac{\partial p_{1D}}{\partial y_D} \right) \delta p_{1D} - \frac{1}{C_D e^{2S}} \frac{\partial p_{1D}}{\partial T_D} \delta p_{1D} \right) dA = 0 \tag{25}$$

Subsection integration is used and we can get:

$$\iint_A \left( \frac{\partial}{\partial x_D} \left( \frac{\partial p_{1D}}{\partial x_D} \delta p_{1D} \right) + \frac{\partial}{\partial y_D} \left( \frac{\partial p_{1D}}{\partial y_D} \delta p_{1D} \right) - \left( \frac{\partial p_{1D}}{\partial x_D} \frac{\partial \delta p_{1D}}{\partial x_D} + \frac{\partial p_{1D}}{\partial y_D} \frac{\partial \delta p_{1D}}{\partial y_D} \right) - \frac{1}{C_D e^{2S}} \frac{\partial p_{1D}}{\partial T_D} \delta p_{1D} \right) dA = 0 \tag{26}$$

From the divergence theorem of Gauss, we can get:

$$\iint_A \left( \frac{\partial}{\partial x_D} \left( \frac{\partial p_{1D}}{\partial x_D} \delta p_{1D} \right) + \frac{\partial}{\partial y_D} \left( \frac{\partial p_{1D}}{\partial y_D} \delta p_{1D} \right) \right) dA = \int_s \delta p_{1D} \frac{\partial p_{1D}}{\partial n} ds \tag{27}$$

Then, the weak forms of these variational equations (23) and (24) can be written as follows:

$$\iint_A \left( \frac{\partial p_{1D}}{\partial x_D} \frac{\partial \delta p_{1D}}{\partial x_D} + \frac{\partial p_{1D}}{\partial y_D} \frac{\partial \delta p_{1D}}{\partial y_D} + \frac{1}{C_D e^{2S}} \frac{\partial p_{1D}}{\partial T_D} \delta p_{1D} \right) dA = \int_s \delta p_{1D} \frac{\partial p_{1D}}{\partial n} ds \tag{28}$$

and

$$\iint_A \left( \frac{\partial p_{2D}}{\partial x_D} \frac{\partial \delta p_{2D}}{\partial x_D} + \frac{\partial p_{2D}}{\partial y_D} \frac{\partial \delta p_{2D}}{\partial y_D} + \frac{1}{DC_D e^{2S}} \frac{\partial p_{2D}}{\partial T_D} \delta p_{2D} \right) dA = \int_s \delta p_{2D} \frac{\partial p_{2D}}{\partial n} ds \tag{29}$$

In the right terms of equations (28) and (29), $s$ is the boundary of computational domain, which means $s$ in equation (28) represents the wellbore boundary$\Gamma_w$, the reservoir boundary$\Gamma_r$ and the cavity's boundary$\Gamma_c$, $s$ in equation (29) represents the cavity's boundary$\Gamma_c$. Therefore, equations (28) and (29) can be rewritten as:

$$\iint_A \left( \frac{\partial p_{1D}}{\partial x_D} \frac{\partial \delta p_{1D}}{\partial x_D} + \frac{\partial p_{1D}}{\partial y_D} \frac{\partial \delta p_{1D}}{\partial y_D} + \frac{1}{C_D e^{2S}} \frac{\partial p_{1D}}{\partial T_D} \delta p_{1D} \right) dA = \int_{\Gamma_w} \delta p_{1D} \frac{\partial p_{1D}}{\partial n} d\Gamma_w + \int_{\Gamma_r} \delta p_{1D} \frac{\partial p_{1D}}{\partial n} d\Gamma_r + \int_{\Gamma_c} \delta p_{1D} \frac{\partial p_{1D}}{\partial n} d\Gamma_c \tag{30}$$

and

$$\iint_A \left( \frac{\partial p_{2D}}{\partial x_D} \frac{\partial \delta p_{2D}}{\partial x_D} + \frac{\partial p_{2D}}{\partial y_D} \frac{\partial \delta p_{2D}}{\partial y_D} + \frac{1}{DC_D e^{2S}} \frac{\partial p_{2D}}{\partial T_D} \delta p_{2D} \right) dA = \int_{\Gamma_c} \delta p_{2D} \frac{\partial p_{2D}}{\partial n} d\Gamma_c \tag{31}$$

The first and second term in the right side of equation (30) can be represented by the wellbore boundary condition equation (17) and the reservoir boundary condition equation (18), respectively. To get the solution of the whole domain, we need to combine equation (30) and equation (31). In the process of combination, equation (31) is multiplied by $M$, then the third term in the right side of equation (30) and the right term of equation (31) can be offset by using the surface conditions between the matrix and the cavity equation (21). Equations (30) and (31) become:

$$\iint_A \left( \frac{\partial p_{1D}}{\partial x_D} \frac{\partial \delta p_{1D}}{\partial x_D} + \frac{\partial p_{1D}}{\partial y_D} \frac{\partial \delta p_{1D}}{\partial y_D} + \frac{1}{C_D e^{2S}} \frac{\partial p_{1D}}{\partial T_D} \delta p_{1D} \right) dA = \int_{\Gamma_w} \delta p_{1D} \left( -1 + \frac{dp_{wD}}{dT_D} \right) d\Gamma_w \tag{32}$$

and

$$\iint_A \left( \frac{\partial p_{2D}}{\partial x_D} \frac{\partial \delta p_{2D}}{\partial x_D} + \frac{\partial p_{2D}}{\partial y_D} \frac{\partial \delta p_{2D}}{\partial y_D} + \frac{1}{DC_D e^{2S}} \frac{\partial p_{2D}}{\partial T_D} \delta p_{2D} \right) M dA = 0 \tag{33}$$

In an element, the interpolations of the variables can be written as:

$$p_{1D} = \sum_{i=1}^{3} N_i(x_D, y_D) p_{1Di}(T_D) \tag{34}$$

$$\delta p_{1D} = \sum_{i=1}^{3} N_i(x_D, y_D) \delta p_{1Di}(T_D) \tag{35}$$

$$p_{2D} = \sum_{i=1}^{3} N_i(x_D, y_D) p_{2Di}(T_D) \tag{36}$$

$$\delta p_{2D} = \sum_{i=1}^{3} N_i(x_D, y_D) \delta p_{2Di}(T_D) \tag{37}$$

where $N$is the shape function of the element. If we use linear interpolated function, we can get:

$$N_i = a_i + b_i x + c_i y \tag{38}$$

where

$$A = \frac{1}{2} \begin{vmatrix} 1 & x_i & y_i \\ 1 & x_j & y_j \\ 1 & x_k & y_k \end{vmatrix} \tag{39}$$

$$a_i = \frac{1}{A} \begin{vmatrix} x_j & y_j \\ x_k & y_k \end{vmatrix} \tag{40}$$

$$b_i = -\frac{1}{A} \begin{vmatrix} 1 & y_j \\ 1 & y_k \end{vmatrix} \tag{41}$$

$$c_i = \frac{1}{A} \begin{vmatrix} 1 & x_j \\ 1 & x_k \end{vmatrix} \tag{42}$$

$x_i, y_i, x_j, y_j, x_k, y_k$are the coordinates of the three vertices ($i$, $j$, $k$) of the triangle.

Substituting equation (34), (35), (36), and (37) into equation (32) and (33), we get:

$$\sum_{i=1}^{3} \sum_{j=1}^{3} A_{ij} \frac{dp_{1Di}}{dT_D} + \sum_{i=1}^{3} \sum_{j=1}^{3} B_{ij} p_{1Di} = \sum_{j=1}^{3} F_j \tag{43}$$

$$\sum_{i=1}^{3} \sum_{j=1}^{3} \frac{A_{ij}}{D} M \frac{dp_{2Di}}{dT_D} + \sum_{i=1}^{3} \sum_{j=1}^{3} M B_{ij} p_{2Di} = 0 \tag{44}$$

where

$$A_{ij} = \iint_A \left( \frac{1}{C_D e^{2S}} N_i N_j \right) dA \tag{45}$$

$$B_{ij} = \iint_A \left( \frac{\partial N_i}{\partial x_D} \frac{\partial N_j}{\partial x_D} + \frac{\partial N_i}{\partial x_D} \frac{\partial N_j}{\partial x_D} \right) dA \tag{46}$$

$$F_j = \int_{\Gamma_w} \left( -1 + \frac{dp_{wD}}{dT_D} \right) N_j d\Gamma_w \tag{47}$$

Equation (43) are the element stiffness equations for elements in the matrix zone and equation (44) are the element stiffness equations for elements in the cavity zone. All the element stiffness equations are integrated to the total stiffness equations which is solved by using SuperLU (Demmel et al., 1999; Li et al., 1999; Li, 2003) to get the pressure of each node at each time point.

## 4. Analysis of the log-log type curves

### 4.1. The WOC model

#### 4.1.1. Effect of the cavity's radius $r_{vD}$

Fig. 6 presents the log-log plot of $p_D$ and $p'_D$ versus $T_D$ for different values of the cavity's radius $r_{vD}$. After the wellbore storage period, the first radial flow of the matrix appears and is identified by a horizontal derivative. When the pressure extends to the cavity, the pressure derivative drops down and is concave upward, which forms a valley because of the high permeability of the cavity. After the valley, the pressure derivative rises back to the horizontal line of the system radial flow. The larger the cavity, the more dramatic the drop in the pressure derivative. The bottom of the valley on the pressure derivative curve moves to the right with the increase in the cavity's radius. The width of the valley is directly proportional to the cavity's radius. The shape of the type curves in the case of the WOC model is very similar to that of the tested type-I curves in Table 1.

Fig. 7 shows the pressure profile of this model. As can be seen, the pressure travels faster along the side of the cavity and forms a terrace in the cavity, which indicates an extremely low pressure gradient because of the high permeability of the cavity.

#### 4.1.2. Effect of distance $d_D$ between the well and the center of the cavity

Fig. 8 shows the log-log plot of $p_D$ and $p'_D$ versus $T_D$ for different values of $d_D$. As can be seen in Fig. 8, when the distance between the well and the cavity increases, the pressure derivative curve begins to decrease at a slower rate, because the time for pressure extending from the well to the cavity is proportional to the distance $d_D$. The smaller the distance, the deeper the valley. This is because as the distance increases, the ratio of the cavity's area to the cavity-affected formation area (Fig. 12) becomes smaller, and its ability to add energy to the formation becomes weaker. When the dimensionless distance between the cavity and the well is less than 80, the first radial flow matrix period will be obscured by the valley of the cavity.

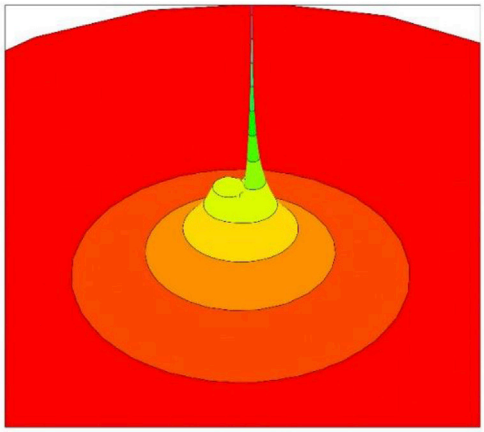

**Fig. 7.** The pressure profile of the WOC model.

#### 4.1.3. Effect of the cavity's mobility ratio M

Fig. 9 shows the log-log plot of $p_D$ and $p'_D$ versus $T_D$ for different values of $M$, which could be 1, 5, 10, 100, and 1 000. For larger mobility ratios, Fig. 9 shows that the amplitude of the derivative valley dips deeper. However, there is a limit to the valley of the amplitude, or how large $M$ may become. For $M = 100$ and $M = 1000$, the derivatives lie on atop each other. This is because of the limiting case that the cavity is empty. When the permeability of the cavity is large enough ($M$ is large), the flow in the cavity will reach the limit of a vacant cavity.

#### 4.1.4. Effect of the diffusivity ratio D

Fig. 10 shows the log-log plot of $p_D$ and $p'_D$ versus $T_D$ for different values of $D$, namely 1, 5, 10, and 20. When $D$ is more than 1, the derivative decreases at first, and then increases, peaking above the 0.5 and then plateauing out. The larger $D$ is, the deeper the derivative decreases and the higher the peak is.

#### 4.1.5. Comparison with dual-porosity model

The most typical characteristic of the type curves for the WOC model is the valley on the derivative curve, which is caused by the high permeability of the cavity. The type-I test pressure curves in Table 1 coincide with type curves of the WOC model and the dual-porosity model. We have pointed out that the dual-porosity model is not suitable for the interpretation of type-I curves. Thus, we make a comparison between the WOC and the dual-porosity models to examine the differences.

We refer to the area under the WOC model as a circle (of radius $r_e$)

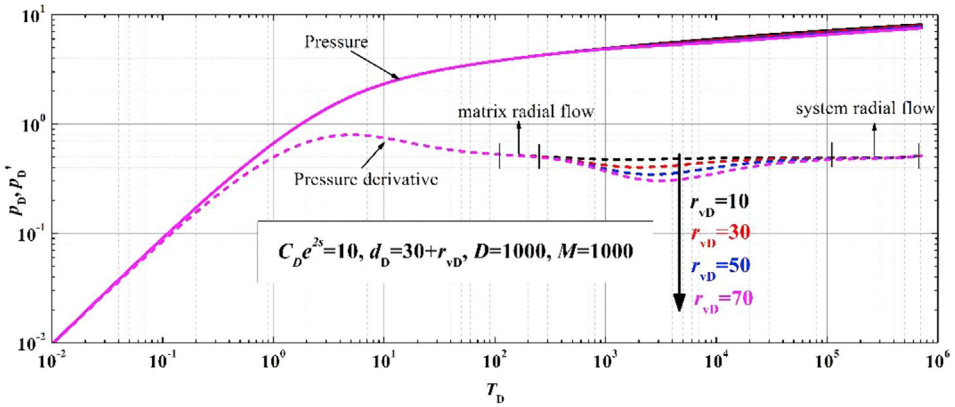


**Fig. 6.** The log-log plot of $p_D$ and $p'_D$ versus $T_D$ in WOC for different values of $r_{vD}$.

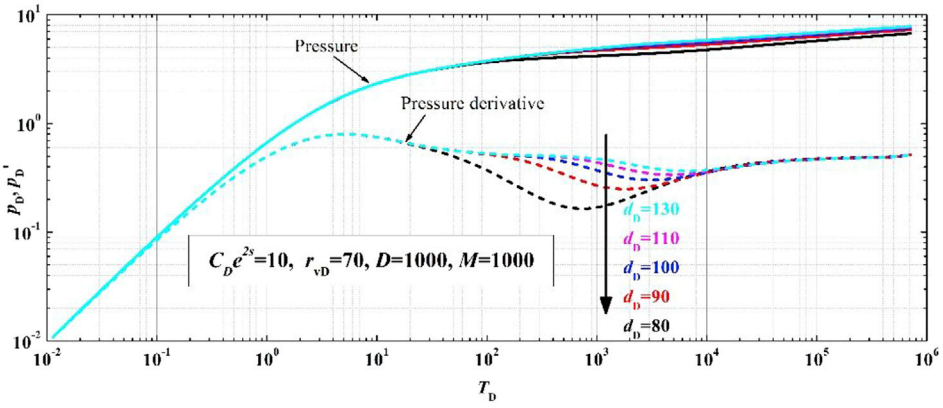


**Fig. 8.** The log-log plot of $p_D$ and $p'_D$ versus $T_D$ in WOC for different values of $d_D$.

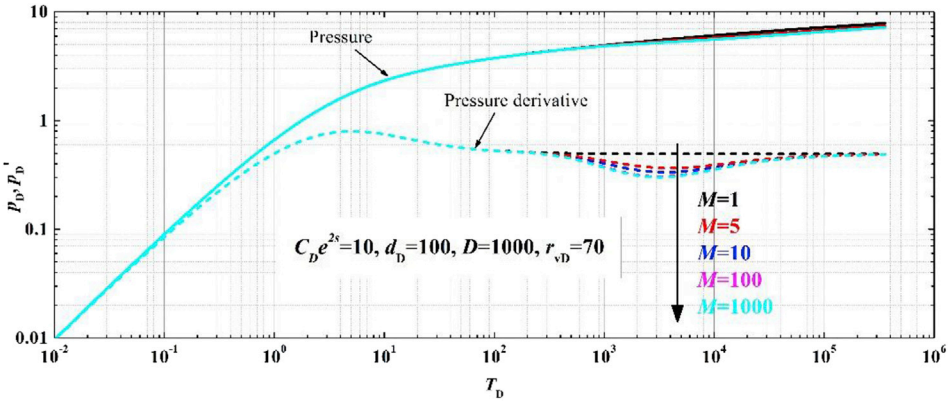


**Fig. 9.** The log-log plot of $p_D$ and $p'_D$ versus $T_D$ in WOC for different values of $M$.

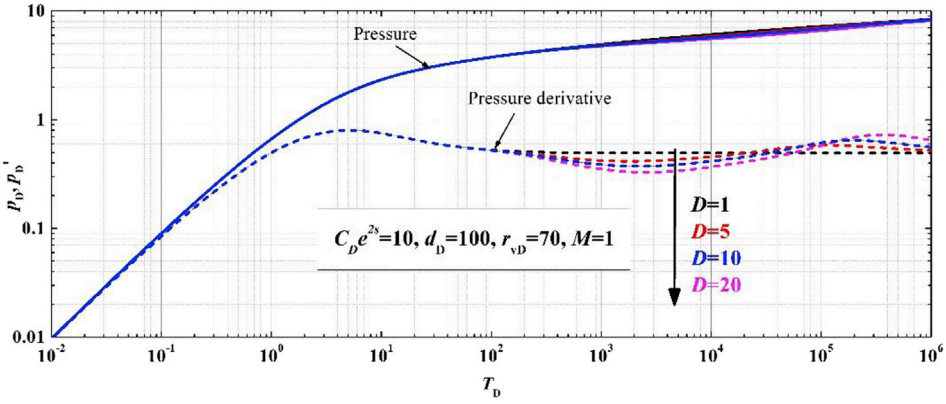


**Fig. 10.** The log-log plot of $p_D$ and $p'_D$ versus $T_D$ in WOC for different values of $D$.

having a closed reservoir boundary. The assumed reservoir and fluid properties of this example are listed in Table 2.

We assume the results of the WOC model are akin to field data and use the dual-porosity model with a slab matrix to implement a well test interpretation to match the log-log plot of the WOC model. The matching plots of the log-log curves are shown in Fig. 11.

From Fig. 11, we can see that the type curves of the dual-porosity model match very well with that of the WOC model. This matching indicates that the matrix is the primary porosity of the dual-porosity model, which represents the fluid flow path, and the secondary porosity is the cavity. The valley on the derivative of the dual-porosity model is created by the energy supplementation caused by the transfer function of the

**Table 2**
Reservoir and fluid properties of the assumed WOC example.

| Variable | Value |
|---|---|
| $p_i$ | 50 MPa |
| $h$ | 10 m |
| $\mu$ | 1 mPa s |
| $B$ | 1 |
| $c_t$ | 0.0035 $MPa^{-1}$ |
| $r_w$ | 0.1 m |
| $r_e$ | 1 000 m |
| $d$ | 120 m |
| $r_v$ | 80 m |

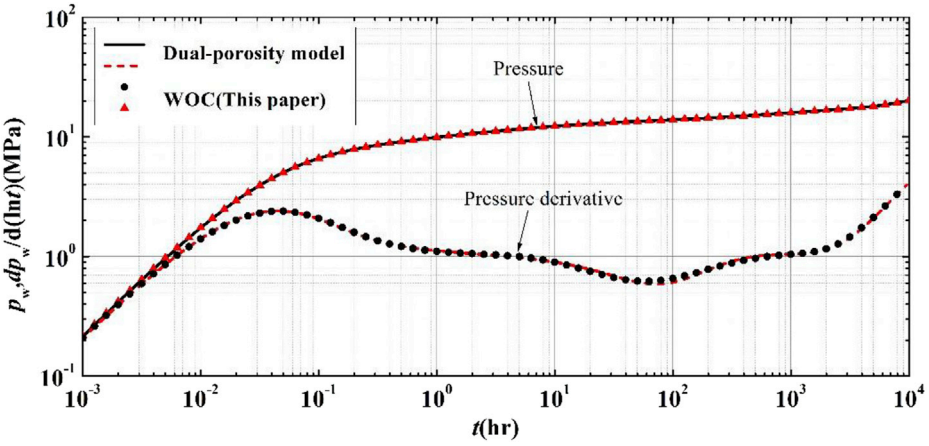


**Fig. 11.** Log-log match plot of the WOC model's results and dual-porosity model (denoted as measured).

secondary porosity. While it is very similar to the mechanism of the WOC model, essential differences remain. In the dual-porosity model, the secondary porosity is full of the reservoir fluid, while the cavity in the WOC model forms only a small part of the reservoir.

Table 3 presents the assumed parameters of the WOC model and the corresponding results of the dual-porosity model from the matching of the type curves. The wellbore storage coefficient and skin factor interpreted by the dual-porosity model are exactly the same as the assumed values of the WOC model. When we use the dual-porosity model to interpret the results for the WOC model, the horizontal derivative indicates the formation capacity ($K{\cdot}h$) of the matrix, and thus, $K_m$ of dual-porosity model is the same as that of the WOC model. Consequently, the reservoir's radius $r_e$ of the dual-porosity model naturally coincides with that of the WOC model.$\omega$ is the storage ratio of primary porosity to total porosity and $\lambda$ is the inter-porosity flow coefficient, which are the characteristic parameters of the dual-porosity model and they control the valley on the derivative curve. A smaller $\omega$ will result in a deeper valley. The above analysis (Figs. 6 and 8) shows the distance from the cavity to the well $d_D$ and the size of the cavity $r_{vD}$ in the WOC model dominate the valley on the derivative. For comparison with the dual-porosity model, we develop an equivalent storage ratio of the cavity according to the definition of the storage ratio in the dual-porosity model. It is the ratio of the area of the cavity to the area of cavity-affecting part, which is shown in Fig. 12.

The equivalent storage ratio of the WOC model is

$$\omega'_v = \frac{\pi r_v^2}{\pi(d+r_v)^2} = \left(\frac{r_v}{d+r_v}\right)^2 \tag{48}$$

Substituting the values in Table 2 into equation (48), we get$\omega'_v = 0.16$, while the storage ratio of the cavity interpreted by the dual-porosity model is $1-\omega = 0.725$, which is much larger than the "real" cavity storage ratio. Therefore, if we use the dual-porosity model to interpret the test pressure for type I, the storage capability of the cavity will be overestimated.

**Table 3**
Well test results of the assumed WOC example using dual-porosity model.

| Variable | Dual-porosity model | WOC |
|---|---|---|
| $C$ | 0.0092 m$^3$/MPa | 0.01 m$^3$/MPa |
| $S$ | 0 | 0 |
| $K_m$ | 10 md | 10 md |
| $K_c$ | / | 100 md |
| $r_e$ | 1 000 m | 1 000 m |
| $\omega$ | 0.275 | / |
| $\lambda$ | 4.81e-7 | / |

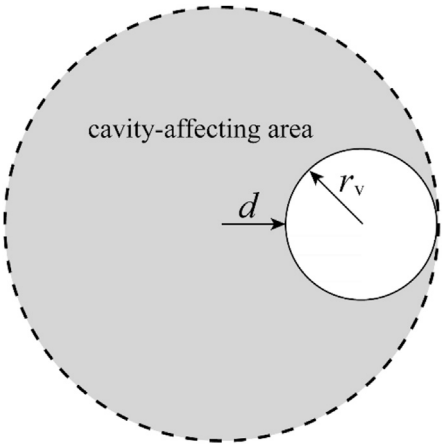


**Fig. 12.** Schematic diagram of the cavity-affecting area and equivalent storage ratio.

### 4.2. The WIC model

#### 4.2.1. Effect of the cave radius $r_{vD}$

The log-log plots of $p_D$ and $p'_D$ versus $T_D$ of the WIC model for different values of $r_{vD}$, which namely 10, 30, and 100, as shown in Fig. 13. When the well is located in the cavity, we apply radial composite model and the inner zone is the cavity. Fig. 13 shows two stabilization lines (zero slope) on the derivative, representing radial flow for the cavity and the matrix. The larger the cavity radius $r_{vD}$, the longer-lasting the radial flow of the cave, and the more delayed the start of the radial flow of the matrix. The shapes of the log-log plots of the WIC model are very similar to that of the type-II test pressure in Table 1. This is because the WIC model is the same as the radial composite model when $d_D = 0$, which means the well is located in the center of the cavity.

#### 4.2.2. Effect of the distance $d_D$ between the well and the center of the cavity

Fig. 14 shows the log-log plot of $p_D$ and $p_D'$ versus $T_D$ for different values of $d_D$, namely 0, 40, 60, and 80. $d_D$ is the distance by which the well deviates from the center of the cavity. If $d_D > 0$, pressure will first reach the side of the cavity closer to the well, and the pressure derivative rises at the end of the first radial flow period. The larger $d_D$, the greater the rise. $d_D$ is the major difference between the WIC and the radial composite models, but it should be noted that the influence of $d_D$ on the derivative is relatively small.

#### 4.2.3. Effect of the cavity's mobility $\boldsymbol{M}$

The log-log plot of $p_D$ and $p_D'$ versus $T_D$ for different values of $M$ is

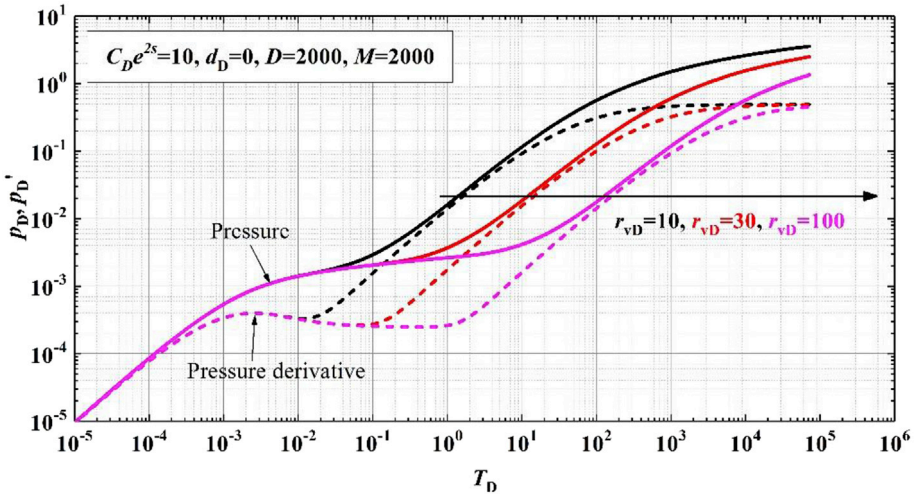


**Fig. 13.** The log-log plot of $p_D$ and $p_D$'versus $T_D$ in WIC for different values of $r_{vD}$.

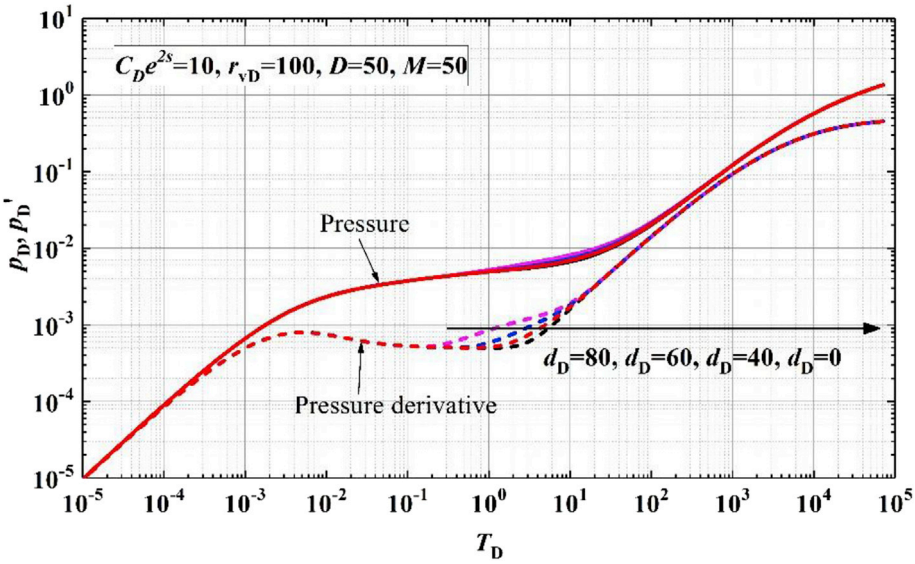


**Fig. 14.** The log-log plot of $p_D$ and $p_D$' versus $T_D$ in WIC for different values of $d_D$

shown in Fig. 15. We can see that the larger the value of $M$, the lower the first stabilization line on the derivative. In the radial composite model, the second stabilization line, rather than the first one, moves, signaling an increase or decrease as $M$ changes. This is because dimensionless pressure in this study was defined by the parameters of the matrix, namely, the outer zone, while the radial composite model's dimensionless pressure is defined with the parameters of the inner zone as a reference.

## 5. Field examples

### 5.1. An example of the WOC model

An oil well named A in the Tarim Oilfield, China began production in December 2009. This well was chosen to represent type I in Table 1. The properties of the oil and the reservoir are listed in Table 4.

A pressure build-up test with a duration of 204 h was performed in June 2010. Before the pressure build-up, the well had produced oil for 4350 h, with an average rate of 57 $m^3$/d. Fig. 16 shows the pressure history during the test. A pressure gradient test was conducted along the wellbore before and after the pressure build-up. The bottom hole pressure was recorded at the frequency of 1 point per second. Due to paucity of space, we deleted the pressure gradient test data and present sparser data here.

The log-log plot of the pressure and pressure derivative is shown in Fig. 17. From the FCU in the first row of Table 1, we note the presence of a cavity near the well but the well is located outside the cavity. The shape of the log-log plot and the FCU both coincide with that of type I. Therefore, we apply the WOC model to interpret the pressure build-up test for Well A.

The first step of interpretation is to build a geometric model using the FCU. The boundary of the cavity is simply determined by the FCU, but the boundary of the reservoir cannot be the boundary of the FCU. If the boundary of the FCU is the boundary of the WOC model, irrespective of whether the boundary is closed or under constant pressure, the derivative of the build-up test will decrease at the end (Bourdet, 2002). However, almost none of the log-log plots of the test pressures in a reservoir have this feature. Therefore, we believe that the boundary of the FCU is not completely closed while the permeability of the area beyond the FCU is extremely small. At this point, we build a geometric model and mesh shown in Fig. 18. We add a large enough closed circle reservoir boundary beyond the FCU, and thus, the boundary response does not occur during the pressure build-up period. We name the added area that lies beyond

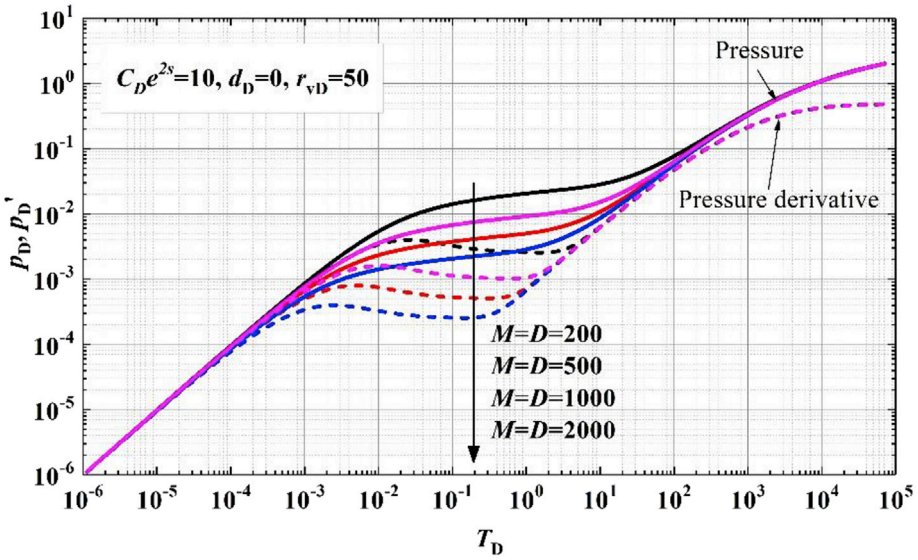


**Fig. 15.** The log-log plot of $p_D$ and $p_D'$ versus $T_D$ in WIC for different values of $M$

**Table 4**
Well-A's properties of the reservoir and the wellbore.

| Parameter | Value |
|---|---|
| $\phi$ | 0.042 |
| $h$ | 67 m |
| $r_w$ | 0.079 m |
| $C_t$ | 0.001144 MPa$^{-1}$ |
| $B$ | 1.12 m$^3$/m$^3$ |
| $\mu$ | 1.49 mPa s |

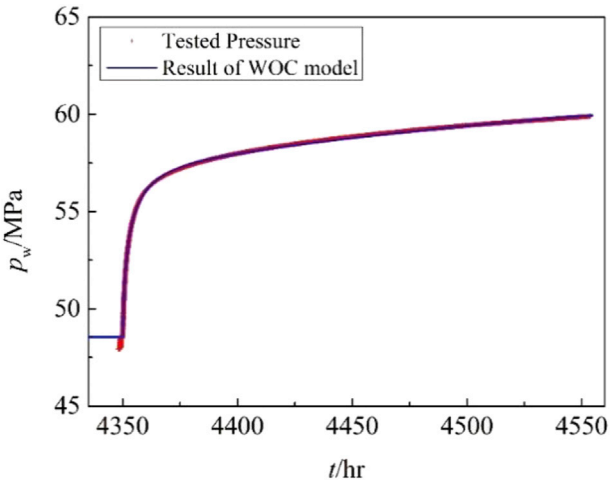


**Fig. 16.** History matching of the tested pressure with the WOC model.

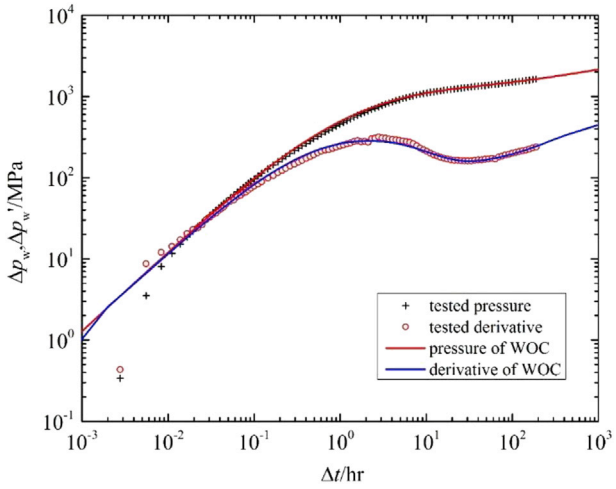


**Fig. 17.** Log-log matching plot of the tested pressure and derivative with the WOC model.

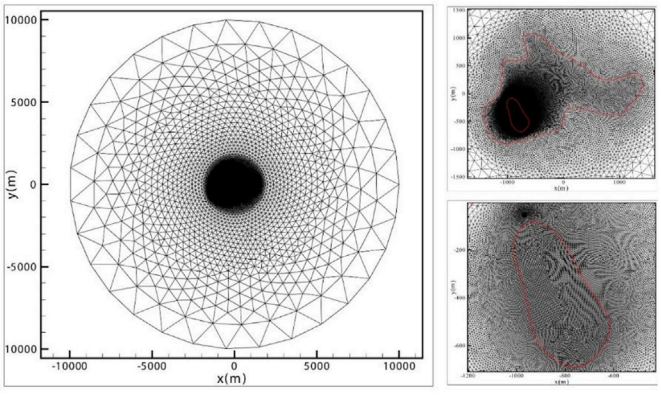


(b) Mesh of the geometric model of well-A

**Fig. 18.** The geometric model and mesh for well-A. The geometric model is generated by the FCU. A large enough background area is added beyond the FCU.

the FCU as "background area." We set the permeability of this area to 0.01 mD. The mesh of the geometric model is presented in Fig. 18-(b). There are 67,739 elements in this model (Fig. 18) and the number of nodes is 33,890. There are 10 time steps distributed as a logarithmic sequence in each of the logarithmic intervals ($10^0$–$10^1$,$10^1$–$10^2$, etc.). One computing time from $10^{-3}$ h–$10^3$ h (60 time steps) is 45 s on a PC with a Intel (R) Core (TM) i7-6 700 @3.4 GHz CPU.

In order to accelerate the process of numerical well test interpretation, first an analytical well test is applied. The results of the analytical well test are used to initialize some of the parameters of the numerical well test model, and then, the parameters of reservoirs ($M$, $D$) and the well ($C$, $S$) are changed empirically to match the log-log plot and history plot of the test pressure. The matching plot of log-log and pressure history

are presented in Figs. 16 and 17. The matching results are listed in Table 5. The wellbore storage coefficient is 0.361 $m^3$/MPa and the skin factor is 2.5 which indicates that Well A is damaged. The cavity's permeability is as large as 827.5 mD, while the permeability of the matrix is 1.2 mD. In this example, the cavity is not circular in shape, and thus, we provide the area rather than the radius. The area of the cavity is $1.07 \times 10^5$ $m^2$ and the closest distance between the well and the boundary of the cavity is 35 m.

### 5.2. An example for the WOC model

We apply the WIC model into the interpretation of test pressure from another well, named Well B, which belongs to type II in Table 1. The drilling is accompanied by leakage of drilling mud of volume 640.92 $m^3$ and a drilling break of 4.6 m. Well B began production in January 2012 and underwent a pressure build-up test that lasted for about 78.33 h in March 2012. Before the pressure build-up, the well had been producing oil for 1425 h at the rate of 25 $m^3$/d. The FCU is shown in the third column and third row of Table 1. The properties of the reservoir and the well are listed in Table 6. The process of well test interpretation is the same as in the previous example of the WOC model, and thus, we show the results here.

Fig. 19 is the matching plot of the bottom hole pressure with the WIC model. The results of the interpretation are listed in Table 7. From the Fig. 19-(b), we can see that there are some oscillations on the pressure derivative. These oscillations may be caused by the gauge drift or tidal effects because the pressure derivative is very sensitive and a little fluctuation on the pressure will cause oscillations on pressure derivative. However, we believe that the oscillations may be caused by the cavity which the well drilled in. The permeability of the cavity is very large and the fluid flow in it is relatively fast, so the flow from the cavity to the wellbore is not very stable, which case the oscillations on derivative, especially in the early time. This is why the oscillations occur on the early time (t < 1hr) in Fig. 19-(b). Also, it should be noticed that the logarithmic coordinate amplification the early data, so this intensifies the oscillation in the early time.

Also, we notice that the matching is not good for some region in Fig. 19-(b) because there are many physical and non-physical effects in the well test that affect the tested curves. The model we use can't include all the effects, especially the non-physical effects such as noise and derivative error.

We can see in Table 7 that the wellbore storage coefficient is 13.6 $m^3$/MPa, which is extremely large. This is because the wellbore is located in the cavity, which increases the wellbore volume equivalently. The wellbore skin factor is −4.46, which is obvious because the simulation considers cavities with high permeability. The cavity's permeability is 3 404 mD. The area of the cavity is $3.98 \times 10^4$ $m^2$.

## 6. Conclusion

In this paper, we classified the log-log plot the test pressure into four types and analyzed the characteristics of each type. From the classification, we concluded that for the cavity that controls the fluid flow, the most widely used dual-porosity model is not appropriate for the interpretation of the well test data in carbonate reservoirs. Then, we developed numerical well test models for both a well drilled outside a cavity and one drilled inside it. The diffusivity equations of the models were solved using the finite-element method. For the model of a well located outside of a cavity, the results showed that a valley on the derivative is formed because of the cavity. The larger the size and permeability of the

**Table 5**
The results of well test interpretation for Well A with WOC.

| Parameter | Value |
|---|---|
| $C$ | 0.361 $m^3$/MPa |
| $S$ | 2.5 |
| $K_c$ | 827.5 mD |
| $K_m$ | 1.2 mD |

**Table 6**
Well B's properties of the reservoir and the wellbore.

| Parameter | Value |
|---|---|
| $\phi$ | 0.0402 |
| $h$ | 43 m |
| $r_w$ | 0.0762 m |
| $C_t$ | 0.00124 $MPa^{-1}$ |
| $B$ | 1.037 $m^3/m^3$ |
| $\mu$ | 2.19 mPa s |

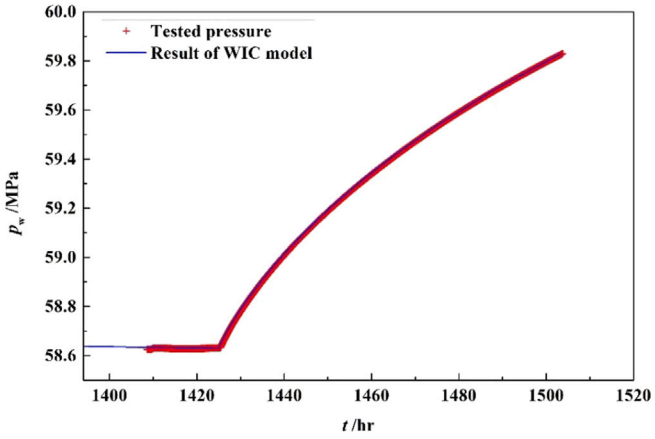


(a) Matching plot of pressure history

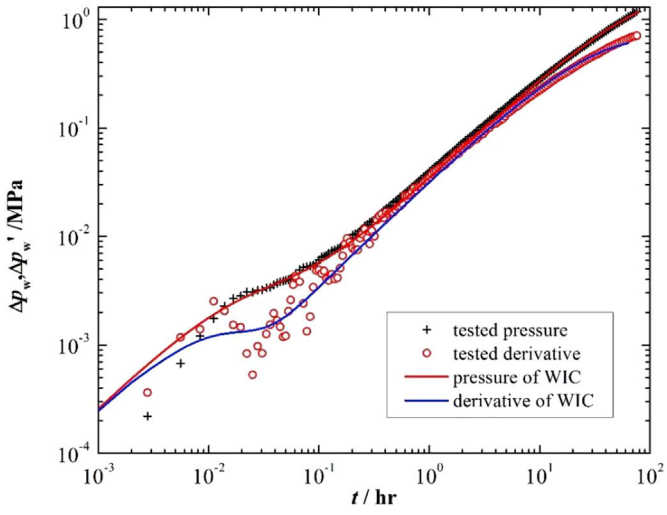


(b) Matching plot of log-log curves of tested pressure

**Fig. 19.** Matching plot of tested pressure with WIC for well-B.

**Table 7**
The results of well test interpretation for Well B with WIC.

| Parameter | Value |
|---|---|
| $C$ | 13.6 $m^3$/MPa |
| $S$ | −4.46 |
| $K_c$ | 3 404 mD |
| $K_m$ | 0.2 mD |

cavity, the deeper the valley. A smaller distance between the well and the cavity also results in a deeper valley. A comparison between the model of a well located outside a cavity and the dual-porosity model showed that although their log-log plots fit inside each other, the physical mechanisms of these two models are totally different. The model of a well located inside of a cavity is the same as the radial composite model, except for the deviated distance of the well from the center of the cavity. This deviated distance causes a small increase of the derivative at the end of the first radial flow.

We applied these models to the interpretation of actual well test data. Two examples, of a well located outside a cavity and a well inside it, were presented to show how the models developed here can be used in the interpretation of pressure build-up tests.

However, it should be pointed out that the model developed in this paper can be only used in the filled cavities which follow Darcy's law. The case of unfilled cavities should use Navier-Stokes equations to describe the fluid flow, which will be discussed in another drafting manuscript. Also, we consider the case of single cavity in the model, but it is easily extended to multiple cavities' case of the type IV in Table 1.

## Acknowledgment

The authors would like to acknowledge the funding by the project (Grant No. 41474119) sponsored by the Natural Science Foundation of China (NSFC).

## References

Barenblatt, G.I., Zheltov, I.P., Kochina, I.N., 1960. Basic concepts in the theory of seepage of homogeneous liquids in fissured rocks [strata]. J. Appl. Math. Mech. 24 (5), 1286–1303. https://doi.org/10.1016/0021-8928(60)90107-6.

Bourdet, D., 2002. Well Test Analysis: the Use of Advanced Interpretation Models, first ed. Elsevier, Amsterdam, pp. 233–235.

Cheng, Q., Xiong, W., Gao, S.-S., Liu, H.-X., 2009. Channeling model of non-steady flow from matrix to insular cavity. Spec. Oil Gas. Reserv. 16, 53–54.

Chu, W.C., Shank, G.D., 1993. A new model for a fractured well in a radial, composite reservoir. SPE Form. Eval. 8 (03), 225–232. SPE-20579-PA. https://doi.org/10.2118/20579-PA.

Civan, F., Rasmussen, M.L., 2001. Asymptotic analytical solutions for imbibition waterfloods in fractured reservoirs. SPE J. 6 (2), 171–181. SPE-71312-PA. https://doi.org/10.2118/71312-PA.

de Swaan, O.A., 1976. Analytic solutions for determining naturally fractured reservoir properties by well testing. SPE J. 16 (03), 117–122. SPE-5346-PA. https://doi.org/10.2118/5346-PA.

Demmel, J.W., Eisenstat, S.C., Gilbert, J.R., et al., 1999. A supernodal approach to sparse partial pivoting. SIAM J. MATRIX Anal. Appl. 20 (3), 720–755. https://doi.org/10.1137/S0895479895291765.

Djatmiko, W., Hansamuit, V., 2010. Well test analysis of multiple matrix - to -fracture fluid transfer in fractured-vuggy reservoir. In: Presented at the International Oil and Gas Conference and Exhibition in China. Beijing, China, 8–10 June. SPE-130557-MS. https://doi.org/10.2118/130557-MS.

Gao, B., Huang, J.J., Yao, J., et al., 2016. Pressure transient analysis of a well penetrating a filled cavity in naturally fractured carbonate reservoirs. J. Pet. Sci. Eng. 145, 392–403.

Gómez, S., Camacho, R., Vásquez, M., et al., 2014. Well test characterization of naturally fractured VuggyReservoirs, with a global optimization method. In: Presented at Offshore Technology Conference-Asia, Kuala Lumpur, Malaysia, 25–28 March. OTC-24762-MS. https://doi.org/10.4043/24762-MS.

He, J.J., Liu, J.D., Lu, X.B., et al., 2009. Recognition and delimitation of fracture and cave units of carbonate reservoir by using seismic attributes analytic technique based on forward model. Oil Geophys. Prospect. 44 (4), 472–477. https://doi.org/10.13810/j.cnki.issn.1000-7210.2009.04.019.

Jiang, H., Song, X., Wang, Y., et al., 2008. Current situation and forecast of the World's carbonate oil and gas exploration and development. Offshore oil. 135 (3), 125–130.

Jiao, F., Dou, Z., 2006a. A Collection of Research Papers on Development of Tahe Oil and Gas. Petroleum Industry Press, Beijing.

Jiao, F., Dou, Z., 2006b. Development Research and Practice on Fracture-caved Carbonate Reservoir in Tahe Oilfield. Petroleum Industry Press, Beijing.

Kazemi, H., 1969. Pressure transient analysis of naturally fractured reservoirs with uniform fracture distribution. SPE J. 9 (4), 451–462. SPE-2156-A. https://doi.org/10.2118/2156-A.

Li, X.S., 2003. An overview of SuperLU: algorithms, implementation, and user interface. ACM Trans. Math. Softw. 31 (3), 302–325. http://escholarship.org/uc/item/1953j20f.

Li, X.S., Demmel, J.W., Li, Sherry, 1999. SuperLU Users' Guide. Lawrence Berkeley National Laboratory.

Li, Y., Zhang, J., Liu, Z.L., et al., 2016. A systematic technique of production forecast for fractured vuggy carbonate gas condensate reservoirs. In: Presented at the SPE Kingdom of Saudi Arabia Technical Symposium and Exhibition, Dammam, Saudi Arabia, 25–28 April. SPE-182776-MS. https://doi.org/10.2118/182776-MS.

Liu, H., Wang, X., 2012. Pressure response characteristics in large scale cavity type reservoir. J. Southwest Pet. Univ. Technol. 34 (4), 94–99. https://doi.org/10.3863/j.issn.1674-5086.2012.04.013.

Liu, L., Sun, Z.D., Wang, H.Y., et al., 2011. 3D seismic attribute optimization technology and application for dissolution caved carbonate reservoir prediction. In: Presented at the SEG Annual Meeting, San Antonio, Texas, 18–23 September. SEG-2011-1968.

Loucks, T.L., Guerrero, E.T., 1961. Pressure drop in a composite reservoir. SPE J. 1 (3), 170–176. SPE-19-PA. https://doi.org/10.2118/19-PA.

Najurieta, H.L., 1980. A theory for pressure transient analysis in naturally fractured reservoirs. J. Pet. Technol. 32 (7), 5–8. SPE-6017-PA. https://doi.org/10.2118/6017-PA.

Nie, R., Jia, Y., Liu, B., et al., 2009. The transient well test analysis of fractured-vuggy triple-porosity reservoir with the quadratic pressure gradient term. In: Presented at the Latin American and Caribbean Petroleum Engineering Conference, Cartagena de Indias, Colombia, 31 May-3 June. SPE-120927-MS. https://doi.org/10.2118/120927-MS.

Ran, Q., Wang, Y., Sun, Y., et al., 2014. Volcanic Gas Reservoir Characterization, first ed. Gulf Professional Publishing, Boston.

Satman, A., Eggenschwiler, M., Tang, R.W.K., et al., 1980a. An analytical study of transient flow in systems with radial discontinuities. In: Presented at the SPE Annual Technical Conference and Exhibition, Dallas, Texas, 21–24 September. SPE-9399-MS. https://doi.org/10.2118/9399-MS.

Satman, A., Eggenschwiler, M., Ramey, H.J., 1980b. Interpretation of injection well pressure transient data in thermal oil recovery. In: Presented at the SPE California Regional Meeting, Los Angeles, California, 9–11 April. SPE-8908-MS. https://doi.org/10.2118/8908-MS.

Schöberl, J., 1997. NETGEN an advancing front 2d/3d-mesh generator based on abstract rules. Comput. Vis. Sci. 1 (1), 41–52. https://doi.org/10.1007/s007910050004.

Stalgorova, K., Mattar, L., 2013. Analytical model for unconventional multifractured composite systems. SPE Res. Eval. Eng 16 (3), 246–256. SPE-162516-PA. https://doi.org/10.2118/162516-PA.

Su, S., Gosselin, O., Parvizi, H., et al., 2013. Dynamic matrix-fracture transfer behavior in dual-porosity models. In: Presented at the EAGE Annual Conference & Exhibition Incorporating SPE Europec, London, UK, 10–13 June. SPE-164855-MS. https://doi.org/10.2118/164855-MS.

Teimoori, A., 2005. Calculation of the Effective Permeability and Simulation of Fluid Flow in Naturally Fractured Reservoirs. PhD thesis. University of New South Wales, Sydney (2005 June).

The SI Metric System of Units And SPE METRIC STANDARD. Society of Petroleum Engineers.

Wang, Z.S., Yao, J., Dai, W.H., 2007. Application of the well test interpretation method for fracture-vug reservoir in tahe oilfield. J. Xi'an Shiyou Univ. 22 (1), 72–74.

Wan, Y.Z., Liu, Y.W., Ouyang, W.P., et al., 2016. Numerical investigation of dual-porosity model with transient transfer function based on discrete-fracture model. Appl. Math. Mech.-Engl 37 (5), 1–16. https://doi.org/10.1007/s10483-016-2075-8.

Warren, J.E., Root, P.J., 1963. The behavior of naturally fractured reservoirs. SPE J. 3 (3), 245–255. SPE-426-PA. https://doi.org/10.2118/426-PA.

Xiao, C., Liu, X., Zhang, C.S., et al., 2010. Characterizing fractured-vuggy carbonate reservoirs quantitatively based on the integration of well and seismic. In: Presented at the SPWLA 51st Annual Logging Symposium, Perth, Australia, 19–23 June. SPWLA-2010-20330.

Yang, F., Wang, X.-H., Liu, H., 2011. Well test interpretation model for wells drilled in cavity of fractured vuggy carbonate reservoirs. Chin. J. Hydrodyn. 26 (3), 278–283. https://doi.org/10.3969/j.issn1000-4874.2010.03.002.

Yao, S.S., Wang, X.Z., Zeng, F.H., et al., 2016. A composite model for multi-stage fractured horizontal wells in heterogeneous reservoirs (Russian). In: Presented at the SPE Russian Petroleum Technology Conference and Exhibition, Moscow, Russia, 24–26 October. SPE-182016-RU. https://doi.org/10.2118/182016-RU.

Zhao, W., Shen, A., Qiao, Z., et al., 2014. Carbonate karst reservoirs of the Tarim Basin, northwest China: types, features, origins, and implications for hydrocarbon exploration. Interpretation 2 (3), SF65–SF90. https://doi.org/10.1190/INT-2013-0177.1.

Zhang, F.-X., Chen, F.-F., Peng, J.-X., Jia, Y.-L., Lei, S.-L., Yang, X.-T., Yang, J.-J., 2009. A well test model for wells drilled in big-size cavity of naturally fractured vuggy carbonate reservoirs. Acta Pet. Sin. 30, 912–915.

Zhu, G.Y., Zou, C.N., Yang, H.J., et al., 2015. Hydrocarbon accumulation mechanisms and industrial exploration depth of large-area fracture-cavity carbonates in the Tarim Basin, Western China. J. Pet. Sci. Eng. 133, 889–907.